Enhanced valley polarization of graphene on *h*-BN under circularly polarized light irradiation

Keisuke Nakagahara[1] and Katsunori Wakabayashi[1,2,3]

[1]*Department of Nanotechnology for Sustainable Energy, School of Science and Technology, Kwansei Gakuin University, Gakuen-Uegahara 1, Sanda 669-1330, Japan*

[2]*National Institute for Materials Science (NIMS), Namiki 1-1, Tsukuba 305-0044, Japan*

[3]*Center for Spintronics Research Network (CSRN), Osaka University, Toyonaka 560-8531, Japan*

(Received 6 June 2022; revised 25 July 2022; accepted 26 July 2022; published 3 August 2022)

Graphene on *h*-BN (G/hBN) has a long period moiré superstructure owing to the lattice mismatch between two materials. The long periodic potential caused by the moiré superstructure induces modulation of the electronic properties of the system. In this paper, we numerically calculate the optical conductivity of G/hBN under circularly polarized light irradiation. The lack of spatial inversion symmetry in G/hBN induces valley polarization. Furthermore, valley polarization becomes most pronounced in the infrared and terahertz regions if the twist angle between two materials is close to zero for the nondoping case, however, it is insensitive to the twist angle for the hole-doped case. These results will serve to design valleytronics devices using G/hBN.

DOI: 10.1103/PhysRevB.106.075403

I. INTRODUCTION

Two-dimensional (2D) atomically thin materials are attracting much attention owing to their high flexibility in controlling the electronic and optical properties to design new functional devices [1–4]. Graphene, a one atomic thickness carbon sheet, is one of the fundamental 2D materials [5]. Graphene has a honeycomb lattice structure, and its electronic states near the Fermi energy are well described by a massless Dirac equation [6,7]. When two graphene materials are overlaid with a slight twisting angle, a moiré superstructure appears and works as a long periodic electronic potential for the Dirac electrons of graphene [8–15], i.e., so-called *twisted bilayer graphene* (TBG). The period of the moiré superstructure becomes larger when decreasing the twist angle. TBG provides attractive properties such as a vanishing Fermi velocity [11], a flat band at the magic angle [16–18], and superconductivity [19–21]. In addition to TBG, a moiré superstructure also appears when different materials are overlaid. Graphene on *h*-BN (G/hBN), i.e., graphene overlaid on hexagonal boron nitride (hBN), has a moiré superstructure owing to the mismatch of lattice constants between the two materials [22–24]. Experiments of G/hBN have revealed many intriguing phenomena such as the Hofstadter butterfly [25,26] and the fractional quantum Hall effect [24,27,28].

Meanwhile, 2D materials with a honeycomb lattice structure such as graphene and hBN have local minima in the conduction band and local maxima in the valence band in the momentum space, which is referred to as a *valley*. Recently, much effort has been devoted to manipulating the valley degree of freedom to encode and process information, i.e., *valleytronics*, which is the valley analog of spintronics [3,29–35]. The irradiation of circularly polarized light onto 2D materials is one of the typical ways to generate valley polarized states [30,36–40]. Since broken spatial inversion symmetry is needed to induce valley polarization, valley polarized states cannot be realized in monolayer graphene which respects spatial inversion symmetry. However, a moiré superlattice potential of G/hBN owing to a lattice mismatch has trigonal symmetry, i.e., no inversion symmetry, resulting in valley polarization. Several groups have recently investigated the electronic properties of G/hBN [41–43], and its optical absorption properties [44–47]. However, the optical properties under circularly polarized light in G/hBN have yet to be investigated. In this paper, we numerically calculate optical conductivity under circularly polarized light irradiation in a G/hBN heterostructure. It is shown that valley polarization is induced in G/hBN owing to the lack of spatial inversion symmetry. Furthermore, the valley polarization becomes most pronounced when the twist angle between graphene and hBN is close to zero for the nondoping case. However, for the hole-doped case, the valley polarization is insensitive to the twist angle.

II. EFFECTIVE MODEL OF GRAPHENE ON h-BN

Figure 1(a) shows the crystal structure of G/hBN with a twist angle $\theta = 0^\circ$, where a moiré superstructure is clearly seen owing to a lattice mismatch. $\boldsymbol{L}_1^{\rm M}$ and $\boldsymbol{L}_2^{\rm M}$ are moiré primitive vectors and the area surrounded by the rhombus indicates a moiré unit cell. The lattice constant of graphene is $a = 0.246$ nm. Though hBN has the same honeycomb lattice structure, the lattice constant of hBN is $a_{\rm hBN} = 0.2504$ nm [42,48], which is slightly larger than graphene. The ratio of the lattice constant between graphene and hBN is $\alpha = a_{\rm hBN}/a \approx 1.018$. When we define $\boldsymbol{a}_1 = a(1, 0)$ and $\boldsymbol{a}_2 = a(1/2, \sqrt{3}/2)$ as the primitive vectors of graphene, the primitive vectors of the hBN layer of G/hBN are defined as $\tilde{\boldsymbol{a}} = \alpha R(\theta)\boldsymbol{a}_i$ $(i = 1, 2)$, where $R(\theta)$ is the rotation matrix by angle θ. We define the reciprocal vectors $\boldsymbol{G}_i$, $\tilde{\boldsymbol{G}}_i$ for graphene and hBN, respectively.

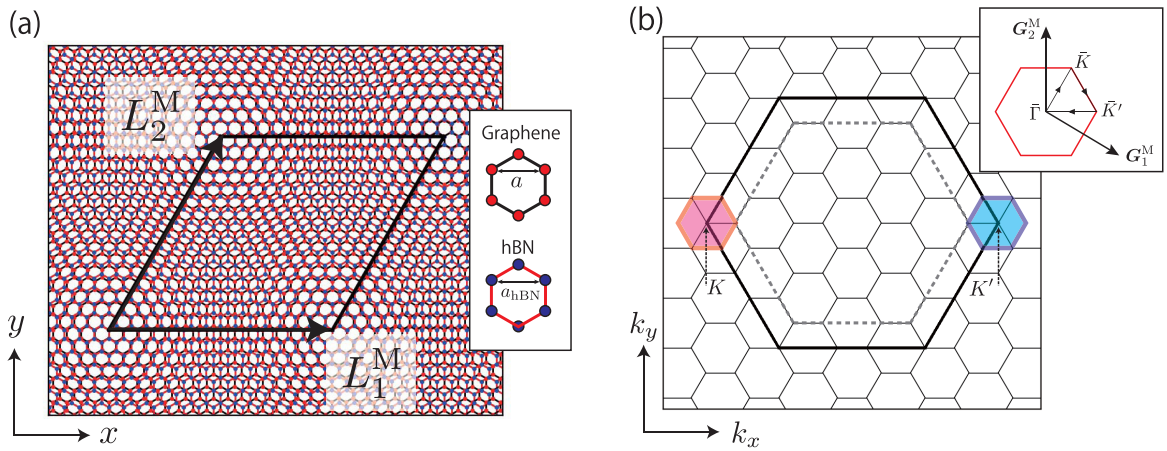

FIG. 1. (a) Crystal structure of G/hBN in real space for twist angle $\theta = 0^\circ$. Here, $a_{\mathrm{hBN}}/a = 16/15$ is used to draw the figure for simplicity. (b) Schematic of reciprocal space. Here, $a_{\mathrm{hBN}}/a = 5/4$ is used to draw the figure for simplicity. The bold black hexagon with a thick line and the gray dashed hexagon show the first BZ for graphene and hBN, respectively. Small hexagons are the moiré BZ. The inset is a zoom of the moiré BZ.

These vectors should satisfy the relation $\boldsymbol{a}_i \cdot \boldsymbol{G}_j = \tilde{\boldsymbol{a}}_i \cdot \tilde{\boldsymbol{G}}_j = 2\pi\delta_{ij}$.

The reciprocal vectors for a moiré period of G/hBN can be defined as

$$\boldsymbol{G}_i^{\mathrm{M}} = [\mathbf{1} - \alpha^{-1}R(\theta)]\boldsymbol{G}_i, \tag{1}$$

where $\mathbf{1}$ is the unit matrix. Note that the period of the moiré superstructure also depends on the twist angle. The corresponding moiré primitive vectors satisfy the relation

$$\boldsymbol{L}_i^{\mathrm{M}} \cdot \boldsymbol{G}_j^{\mathrm{M}} = 2\pi\delta_{ij}. \tag{2}$$

A long periodic potential appears due to the moiré superstructure and affects the electronic states of G/hBN. Figure 1(b) shows the schematic of reciprocal space for G/hBN. The bold black hexagon with a thick line and the gray dashed hexagon show the first Brillouin zone (BZ) for graphene and hBN, respectively. The small hexagons are the moiré BZ spanned by $\boldsymbol{G}_1^{\mathrm{M}}$ and $\boldsymbol{G}_2^{\mathrm{M}}$. The inset is the zoom of the moiré BZ, where the $\bar{\Gamma}$ point means the original K (K') point of graphene. In the continuum model, K and K' valleys are treated independently, and the energy bands can be separately plotted in the BZ centered at K (magenta hexagon) and that centered at K' (cyan hexagon).

The electronic states near the Fermi energy of G/hBN are governed by the electronic states of graphene near the K and K' points. In this paper, we employ an effective continuum model to calculate the eigenenergies and eigenfunctions of G/hBN [42]. The K points of graphene are located at $K_\xi = -\xi(2\boldsymbol{G}_1 + \boldsymbol{G}_2)/3$, where $\xi = \pm 1$ for K and K', respectively. The Dirac Hamiltonian of monolayer graphene near K_ξ can be written as

$$H_{\mathrm{G}} = -\hbar v \boldsymbol{k} \cdot \boldsymbol{\sigma}_{\boldsymbol{\xi}}, \tag{3}$$

where $\boldsymbol{k} = (k_x, k_y)$ is the wave number measured from the K_ξ point, and $\boldsymbol{\sigma}_{\boldsymbol{\xi}} = (\xi\sigma_x, \sigma_y)$ with Pauli matrices σ_x and σ_y. Here, H_{G} is a 2×2 matrix for the basis $\{A_\xi, B_\xi\}$, i.e., the sublattice degree of freedom of graphene. The parameter v is the group velocity of the Dirac cone, which is given as $v = 0.80 \times 10^6$ m/s [42]. By eliminating the basis for hBN using second-order perturbation theory, the effective 2×2 Hamiltonian of G/hBN is written as

$$H_{\mathrm{G/hBN}} = H_{\mathrm{G}} + V_{\mathrm{hBN}}, \tag{4}$$

where V_{hBN} is the long periodic moiré potential including the effect of hBN. V_{hBN} is given as

$$\begin{aligned} V_{\mathrm{hBN}} = V_0 \begin{pmatrix} 1 & 0 \\ 0 & 1 \end{pmatrix} + \Bigg\{ V_1 e^{i\xi\psi} \Bigg[\begin{pmatrix} 1 & \omega^{-\xi} \\ 1 & \omega^{-\xi} \end{pmatrix} e^{i\xi \boldsymbol{G}_1^{\mathrm{M}} \cdot \boldsymbol{r}} \\ + \begin{pmatrix} 1 & \omega^{\xi} \\ \omega^{\xi} & \omega^{-\xi} \end{pmatrix} e^{i\xi \boldsymbol{G}_2^{\mathrm{M}} \cdot \boldsymbol{r}} \\ + \begin{pmatrix} 1 & 1 \\ \omega^{-\xi} & \omega^{-\xi} \end{pmatrix} e^{i\xi \boldsymbol{G}_3^{\mathrm{M}} \cdot \boldsymbol{r}} \Bigg] + \mathrm{H.c.} \Bigg\}, \end{aligned}$$

where $\boldsymbol{G}_3^{\mathrm{M}} = -(\boldsymbol{G}_1^{\mathrm{M}} + \boldsymbol{G}_2^{\mathrm{M}})$, $v = 0.80 \times 10^6$ m/s, $V_0 = 0.0289$ eV, $V_1 = 0.0210$ eV, and $\psi = -0.29$ (rad) [42]. Owing to V_{hBN}, a state at $\boldsymbol{k}$ is related to the other states at $\boldsymbol{k} + n_1\boldsymbol{G}_1^{\mathrm{M}}$, $\boldsymbol{k} + n_2\boldsymbol{G}_2^{\mathrm{M}}$, and $\boldsymbol{k} + n_3\boldsymbol{G}_3^{\mathrm{M}}$, where n_1, n_2, n_3 are integers. In the numerical calculation for optical conductivity, we have taken up to second nearest reciprocal lattices, i.e., 19 independent reciprocal lattice vectors, which is enough to discuss the low-energy properties of the G/hBN system. Thus, the matrix size for the numerical calculations is 38×38.

Figure 2 shows the energy band structure of G/hBN obtained by using the continuum model. When the twist angle gets smaller, the electronic states of G/hBN are modulated by a long periodic moiré potential. At the Brillouin zone boundary, energy band gaps appear in valence bands caused by Bragg scattering where Bloch waves are mixed by the moiré periodic potential. Owing to the moiré periodic potential, the energy band gap opens about 20 meV at the hole band side. The position of the energy band gap goes down with increasing the twist angle. Also, it is noted that a tiny energy band gap with 2 meV is also opened at $E = 0$.

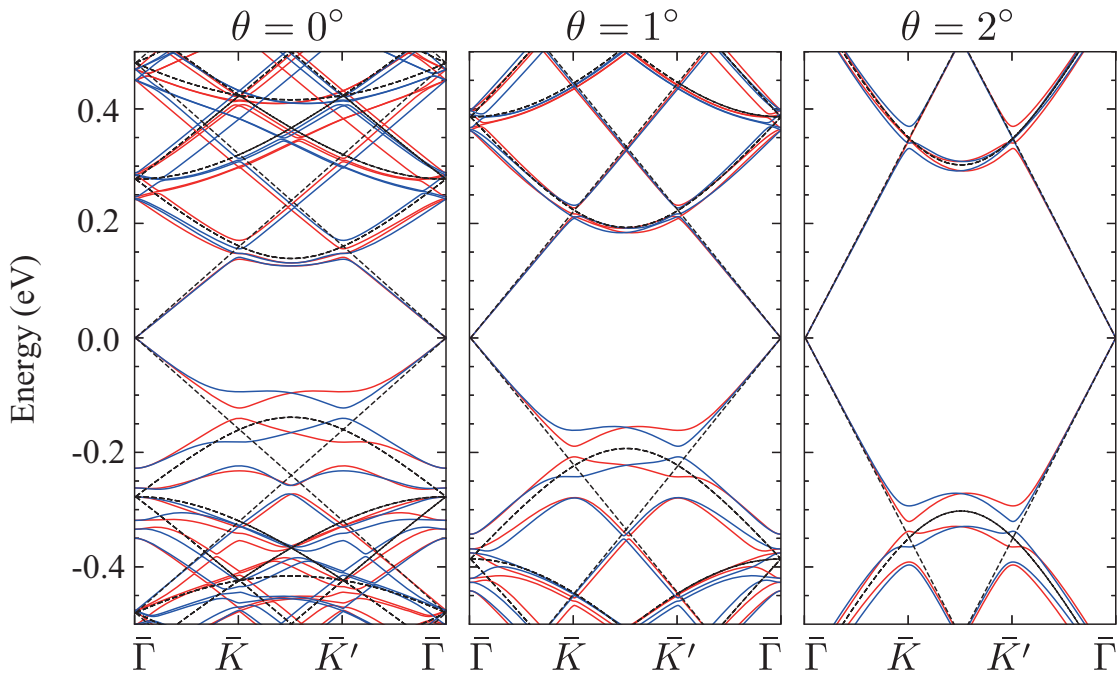

FIG. 2. Energy band structure of G/hBN. Magenta (cyan) bands show the energy bands for the K (K') valley and the black dashed lines are the energy bands of monolayer graphene.

III. OPTICAL PROPERTIES OF GRAPHENE ON h-BN

We use the Kubo formula to calculate the optical conductivity of G/hBN. According to the linear response theory [49], optical conductivity under light irradiation which has a frequency ω is given by

$$\sigma(\omega) = \frac{g_s g_v e^2}{i\hbar S} \sum_{i,j} \sum_{\boldsymbol{k}} \frac{f(E_{\boldsymbol{k}i}) - f(E_{\boldsymbol{k}j})}{E_{\boldsymbol{k}j} - E_{\boldsymbol{k}i}} \times \frac{|\boldsymbol{e} \cdot \langle \psi_{\boldsymbol{k}j} | \nabla_{\boldsymbol{k}} H | \psi_{\boldsymbol{k}i} \rangle|^2}{E_{\boldsymbol{k}j} - E_{\boldsymbol{k}i} - \hbar\omega - i\eta}, \tag{5}$$

where g_s (g_v) is the spin (valley) degree of freedom, i, j are band indices, $\boldsymbol{k}$ is the wave number, $E_{\boldsymbol{k}i}$ is the eigenenergy for band index i, $\psi_{\boldsymbol{k}i}$ is the eigenfunction for band index i, S is the area of the system, and $f(E)$ is the Fermi-Dirac distribution function. η is an infinitesimally small real number. The vector $\boldsymbol{e}$ is the polarization vector of incident light. Under left-handed circularly polarized light (LCP) irradiation, we use

$$\boldsymbol{e}_{\mathrm{LCP}} = \frac{1}{\sqrt{2}}(1, i), \tag{6}$$

and under right-handed circularly polarized light (RCP) irradiation, we use

$$\boldsymbol{e}_{\mathrm{RCP}} = \frac{1}{\sqrt{2}}(1, -i). \tag{7}$$

The matrix element of the interband transition $\langle \psi_{\boldsymbol{k}j} | \nabla_{\boldsymbol{k}} H | \psi_{\boldsymbol{k}i} \rangle$ is related to the dipole vector $\boldsymbol{D}(\boldsymbol{k})$,

$$\boldsymbol{D}(\boldsymbol{k}) := \langle \psi_{\boldsymbol{k}j} | \nabla_{\boldsymbol{r}} | \psi_{\boldsymbol{k}i} \rangle \tag{8}$$

$$= \frac{i}{\hbar} \langle \psi_{\boldsymbol{k}j} | \boldsymbol{p} | \psi_{\boldsymbol{k}i} \rangle \tag{9}$$

$$= i\frac{m}{\hbar^2} \langle \psi_{\boldsymbol{k}j} | \nabla_{\boldsymbol{k}} H | \psi_{\boldsymbol{k}i} \rangle, \tag{10}$$

where $\psi_{\boldsymbol{k}i}$ is a state of the valence band and $\psi_{\boldsymbol{k}j}$ is a state of the conduction band, respectively. Here, $\boldsymbol{p} = -i\hbar\nabla_{\boldsymbol{r}}$ is the momentum operator and m is the mass of the electron. The dipole vector $\boldsymbol{D}(\boldsymbol{k})$ is a vector quantity which is composed of complex values. When the real and imaginary parts of the dipole vector are mutually orthogonal, the circular dichroism under circularly polarized light irradiation occurs [50–52]. For monolayer graphene, the behavior of the dynamical conductivity for a massless Dirac electron becomes a constant value at the universal conductivity [53,54],

$$\sigma_{\mathrm{mono}} = \frac{g_s g_v}{16} \frac{e^2}{\hbar}. \tag{11}$$

In the following, we scale the optical conductivity of G/hBN by using σ_{mono} as

$$\frac{\sigma(\omega)}{\sigma_{\mathrm{mono}}} = \frac{16}{iS^{\mathrm{M}}} \sum_{i,j} \sum_{\boldsymbol{k}} \frac{f(E_{\boldsymbol{k}i}) - f(E_{\boldsymbol{k}j})}{E_{\boldsymbol{k}j} - E_{\boldsymbol{k}i}} \times \frac{|\boldsymbol{e} \cdot \langle \psi_{\boldsymbol{k}j} | \nabla_{\boldsymbol{k}} H | \psi_{\boldsymbol{k}i} \rangle|^2}{E_{\boldsymbol{k}j} - E_{\boldsymbol{k}i} - \hbar\omega - i\eta}, \tag{12}$$

where S^{M} is the area of the moiré periodic unit cell of G/hBN.

Let us consider the optical conductivity of nondoped G/hBN under circularly polarized light irradiation for a twist angle $\theta = 0°$, where the Fermi energy E_{F} is 0 eV. Figure 3(a) shows the optical conductivity of nondoped G/hBN for a Hamiltonian with $\xi = +1$. The conductivity depends on the direction of rotation of circularly polarized light, especially in the infrared and terahertz regions. In particular, for a photon energy less than 0.1 eV, the difference between LCP and RCP becomes larger. In this energy region, the interband transition from valence to conduction bands dominates. Figure 3(b) shows the distribution of dipole vectors for the nondoped case,

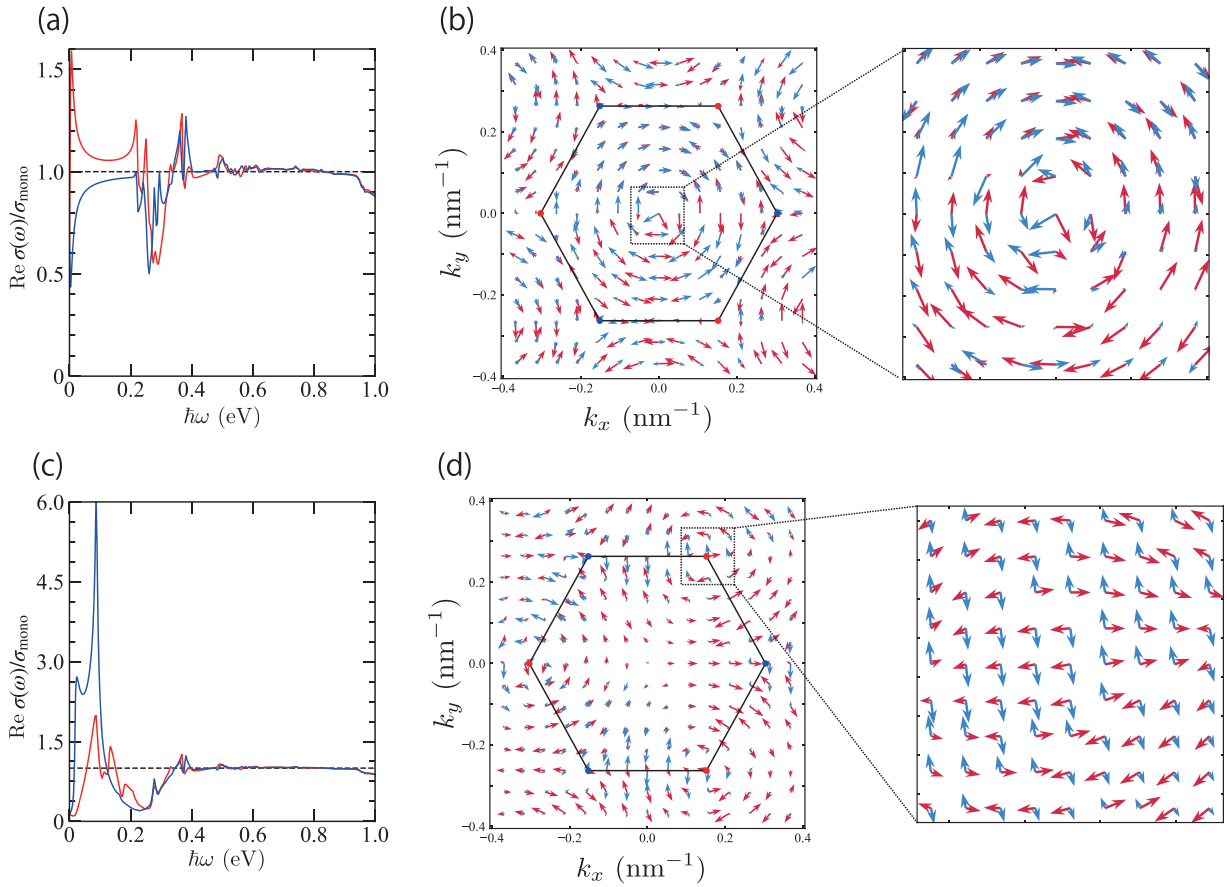

FIG. 3. (a) Optical conductivity of G/hBN for $\xi = 1$ and $E_{\rm F} = 0.0$ eV under circularly polarized light, where the twist angle θ is 0°. The magenta (cyan) curve is the conductivity for LCP (RCP). (b) Distribution of dipole vectors for an interband transition near the Fermi energy $E_{\rm F} = 0.0$ eV in momentum space. The magenta (cyan) arrows are the real (imaginary) parts of the dipole vectors. The black hexagon is the moiré BZ and the magenta (cyan) dots at the hexagon corners are the $\bar{K}$ ($\bar{K}'$) points. (c) Optical conductivity of G/hBN for $E_{\rm F} = -0.13$ eV, where the twist angle θ is 0°. (d) Distribution of dipole vectors for an interband transition near the Fermi energy $E_{\rm F} = -0.13$ eV in momentum space.

i.e., $E_{\rm F} = 0.0$ eV. It is clearly seen that the real and imaginary parts of the dipole vectors are orthogonal at the $\bar{\Gamma}$ point. Thus, the circular dichroism is induced by the irradiation of circularly polarized light, and is responsible for the electron near the $\bar{\Gamma}$ point. For the plot of the dipole-dipole vectors of Eq. (10), we have used the states of the highest valence subband as $\psi_{\boldsymbol{k}i}$ below $E_{\rm F} = 0.0$ eV, and the states of the lowest conduction subband as $\psi_{\boldsymbol{k}j}$ above $E_{\rm F} = 0.0$.

Next, we shall consider the optical conductivity of hole-doped G/hBN. Figure 3(c) shows the optical conductivity with the Fermi energy $E_{\rm F} = -0.13$ eV, i.e., hole doping. In the region of $\omega < 0.1$ eV, the difference in the optical conductivities between LCP and RCP becomes much larger than the nondoping case. As shown in Fig. 3(d), the real and imaginary parts of the dipole vectors are mutually orthogonal at the $\bar{K}$ and $\bar{K}'$ points, which are responsible for the circular dichroism. The results for a Hamiltonian with $\xi = -1$ are obtained by converting LCP (RCP) to RCP (LCP), because the K' states of graphene have opposite chirality to the K states. Here, for the plot of the dipole-dipole vectors of Eq. (10), we have used the states of the highest occupied subband as $\psi_{\boldsymbol{k}i}$ below $E_{\rm F} = -0.13$ eV, and the states of the lowest unoccupied subband as $\psi_{\boldsymbol{k}j}$ above $E_{\rm F} = -0.13$ eV.

Since the optical conductivity depends on the direction of rotation of circularly polarized light, valley-selective electron excitation is possible in G/hBN. Here, we define the valley polarization for each valley as the difference in the conductivity between LCP and RCP,

$$P(\omega) = \frac{\sigma_{\rm L} - \sigma_{\rm R}}{\sigma_{\rm L} + \sigma_{\rm R}}, \quad -1 \leqslant P(\omega) \leqslant 1, \tag{13}$$

where $\sigma_{\rm L}$ and $\sigma_{\rm R}$ are the optical conductivities under LCP and RCP, respectively. The positive (negative) value of $P(\omega)$ means that the electron at the valley is easy to excite by LCP (RCP). Figures 4(a) and 4(b) show the photon energy dependence of valley polarization for the nondoping case and hole-doped case, respectively. In these figures, the value of $P(\omega)$ is shifted by $+1$ per 1° of twist angle. The black, magenta, and cyan curves indicate the case of twist angle $\theta = 0°, 1°, 2°$. For the nondoping case, a valley polarization value of less than 0.1 eV has a maximum value for $\theta = 0°$ and it is decreasing with an increase of the twist angle. These results indicate that the electronic properties of G/hBN approach the electronic states of monolayer graphene with an increase of the twist angle. On the other hand, a valley polarization peak of less than 0.1 eV for the hole-doped case remains even

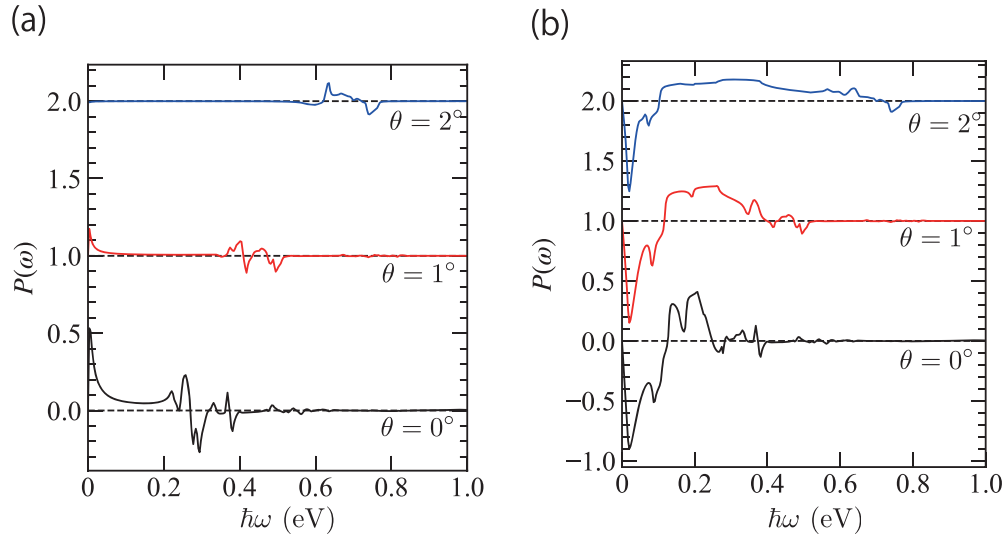

FIG. 4. (a) Photon energy dependence of valley polarization ($E_F = 0$ for several different twist angles, eV). The black dashed lines indicate the $P(\omega) = 0$ line. (b) Photon energy dependence of valley polarization for the hole-doped case, where the Fermi energy is set in the band gap of the valence band at the $\bar{K}$ point. Fermi energies are set as $E_F = -0.13$ eV for $\theta = 0°$, $E_F = -0.20$ eV for $\theta = 1°$, and $E_F = -0.33$ eV for $\theta = 2°$.

though the twist angle becomes larger. The common peak of valley polarization comes from an interband transition across the Fermi energy E_F at the $\bar{K}$ point.

IV. SUMMARY

In this paper, we have numerically calculated the optical conductivity of G/hBN under circularly polarized light irradiation. The optical conductivity of G/hBN changes its behavior depending on the direction of rotation of circularly polarized light due to the broken spatial inversion symmetry of the system. By analyzing the dipole vectors, we have confirmed that the real and imaginary parts of the dipole vectors are mutually orthogonal. Thus, we can explain that the electron for each valley can be selectively excited by using a certain direction of circularly polarized light irradiation. These results indicate that G/hBN can cause valley polarization by circularly polarized light irradiation. Also, we confirmed that the value of valley polarization of G/hBN depends not only on the twist angle but also on the Fermi energy. For the nondoping case, the peak of valley polarization for a photon energy of less than 0.1 eV vanishes with increasing twist angle. On the other hand, for the hole-doped case, it remains even though the twist angle becomes larger. These results will serve to design valleytronics devices using G/hBN.

ACKNOWLEDGMENTS

This work was supported by JSPS KAKENHI (No. JP21H01019, No. 22H05473, and No. JP18H01154) and JST CREST (No. JPMJCR19T1).

[1] K. S. Novoselov, A. Mishchenko, A. Carvalho, and A. H. Castro Neto, 2D materials and van der Waals heterostructures, Science **353**, aac9439 (2016).

[2] S. Das, J. A. Robinson, M. Dubey, H. Terrones, and M. Terrones, Beyond graphene: Progress in novel two-dimensional materials and van der Waals solids, Annu. Rev. Mater. Res. **45**, 1 (2015).

[3] J. R. Schaibley, H. Yu, G. Clark, P. Rivera, J. S. Ross, K. L. Seyler, W. Yao, and X. Xu, Valleytronics in 2D materials, Nat. Rev. Mater **1**, 16055 (2016).

[4] M. Zeng, Y. Xiao, J. Liu, K. Yang, and L. Fu, Exploring two-dimensional materials toward the next-generation circuits: From monomer design to assembly control, Chem. Rev. **118**, 6236 (2018).

[5] A. H. Castro Neto, F. Guinea, N. M. R. Peres, K. S. Novoselov, and A. K. Geim, The electronic properties of graphene, Rev. Mod. Phys. **81**, 109 (2009).

[6] H. Ajiki and T. Ando, Electronic states of carbon nanotubes, J. Phys. Soc. Jpn. **62**, 1255 (1993).

[7] T. Ando, T. Nakanishi, and R. Saito, Berry's phase and absence of back scattering in carbon nanotubes, J. Phys. Soc. Jpn. **67**, 2857 (1998).

[8] J. M. B. Lopes dos Santos, N. M. R. Peres, and A. H. Castro Neto, Graphene Bilayer with a Twist: Electronic Structure, Phys. Rev. Lett. **99**, 256802 (2007).

[9] G. Trambly de Laissardière, D. Mayou, and L. Magaud, Localization of Dirac electrons in rotated graphene bilayers, Nano Lett. **10**, 804 (2010).

[10] E. J. Mele, Commensuration and interlayer coherence in twisted bilayer graphene, Phys. Rev. B **81**, 161405(R) (2010).

[11] R. Bistritzer and A. H. MacDonald, Moiré bands in twisted double-layer graphene, Proc. Natl. Acad. Sci. USA **108**, 12233 (2011).

[12] E. Suárez Morell, J. D. Correa, P. Vargas, M. Pacheco, and Z. Barticevic, Flat bands in slightly twisted bilayer graphene: Tight-binding calculations, Phys. Rev. B **82**, 121407(R) (2010).
[13] P. Moon and M. Koshino, Energy spectrum and quantum Hall effect in twisted bilayer graphene, Phys. Rev. B **85**, 195458 (2012).
[14] J. M. B. Lopes dos Santos, N. M. R. Peres, and A. H. Castro Neto, Continuum model of the twisted graphene bilayer, Phys. Rev. B **86**, 155449 (2012).
[15] P. Moon and M. Koshino, Optical absorption in twisted bilayer graphene, Phys. Rev. B **87**, 205404 (2013).
[16] M. I. B. Utama, R. J. Koch, K. Lee, N. Leconte, H. Li, S. Zhao, L. Jiang, J. Zhu, K. Watanabe, T. Taniguchi, P. D. Ashby, A. Weber-Bargioni, A. Zettl, C. Jozwiak, J. Jung, E. Rotenberg, A. Bostwick, and F. Wang, Visualization of the flat electronic band in twisted bilayer graphene near the magic angle twist, Nat. Phys. **17**, 184 (2021).
[17] S. Lisi, X. Lu, T. Benschop, T. A. d. Jong, P. Stepanov, J. R. Duran, F. Margot, I. Cucchi, E. Cappelli, A. Hunter, A. Tamai, V. Kandyba, A. Giampietri, A. Barinov, J. Jobst, V. Stalman, M. Leeuwenhoek, K. Watanabe, T. Taniguchi, L. Rademaker *et al.*, Observation of flat bands in twisted bilayer graphene, Nat. Phys. **17**, 189 (2021).
[18] K. Sato, N. Hayashi, T. Ito, N. Masago, M. Takamura, M. Morimoto, T. Maekawa, D. Lee, K. Qiao, J. Kim, K. Nakagahara, K. Wakabayashi, H. Hibino, and W. Norimatsu, Observation of a flat band and bandgap in millimeter-scale twisted bilayer graphene, Commun. Mater. **2**, 117 (2021).
[19] Y. Cao, V. Fatemi, A. Demir, S. Fang, S. L. Tomarken, J. Y. Luo, J. D. Sanchez-Yamagishi, K. Watanabe, T. Taniguchi, E. Kaxiras, R. C. Ashoori, and P. Jarillo-Herrero, Correlated insulator behaviour at half-filling in magic-angle graphene superlattices, Nature (London) **556**, 80 (2018).
[20] Y. Cao, V. Fatemi, S. Fang, K. Watanabe, T. Taniguchi, E. Kaxiras, and P. Jarillo-Herrero, Unconventional superconductivity in magic-angle graphene superlattices, Nature (London) **556**, 43 (2018).
[21] M. Yankowitz, S. Chen, H. Polshyn, Y. Zhang, K. Watanabe, T. Taniguchi, D. Graf, A. F. Young, and C. R. Dean, Tuning superconductivity in twisted bilayer graphene, Science **363**, 1059 (2019).
[22] G. J. Slotman, M. M. van Wijk, P.-L. Zhao, A. Fasolino, M. I. Katsnelson, and S. Yuan, Effect of Structural Relaxation on the Electronic Structure of Graphene on Hexagonal Boron Nitride, Phys. Rev. Lett. **115**, 186801 (2015).
[23] M. M. van Wijk, A. Schuring, M. I. Katsnelson, and A. Fasolino, Moiré Patterns as a Probe of Interplanar Interactions for Graphene on *h*-BN, Phys. Rev. Lett. **113**, 135504 (2014).
[24] M. Yankowitz, Q. Ma, P. Jarillo-Herrero, and B. J. LeRoy, van der Waals heterostructures combining graphene and hexagonal boron nitride, Nat. Rev. Phys. **1**, 112 (2019).
[25] C. R. Dean, L. Wang, P. Maher, C. Forsythe, F. Ghahari, Y. Gao, J. Katoch, M. Ishigami, P. Moon, M. Koshino, T. Taniguchi, K. Watanabe, K. L. Shepard, J. Hone, and P. Kim, Hofstadter's butterfly and the fractal quantum Hall effect in moiré superlattices, Nature (London) **497**, 598 (2013).
[26] B. Hunt, J. D. Sanchez-Yamagishi, A. F. Young, M. Yankowitz, B. J. LeRoy, K. Watanabe, T. Taniguchi, P. Moon, M. Koshino, P. Jarillo-Herrero, and R. C. Ashoori, Massive Dirac fermions and Hofstadter butterfly in a van der Waals heterostructure, Science **340**, 1427 (2013).
[27] L. Wang, Y. Gao, B. Wen, Z. Han, T. Taniguchi, K. Watanabe, M. Koshino, J. Hone, and C. R. Dean, Evidence for a fractional fractal quantum Hall effect in graphene superlattices, Science **350**, 1231 (2015).
[28] L. Balents, C. R. Dean, D. K. Efetov, and A. F. Young, Superconductivity and strong correlations in moiré flat bands, Nat. Phys. **16**, 725 (2020).
[29] A. Rycerz, J. Tworzydo, and C. W. J. Beenakker, Valley filter and valley valve in graphene, Nat. Phys. **3**, 172 (2007).
[30] D. Xiao, G.-B. Liu, W. Feng, X. Xu, and W. Yao, Coupled Spin and Valley Physics in Monolayers of MoS_2 and Other Group-VI Dichalcogenides, Phys. Rev. Lett. **108**, 196802 (2012).
[31] X. Xu, W. Yao, D. Xiao, and T. F. Heinz, Spin and pseudospins in layered transition metal dichalcogenides, Nat. Phys. **10**, 343 (2014).
[32] Y. P. Shkolnikov, E. P. De Poortere, E. Tutuc, and M. Shayegan, Valley Splitting of AlAs Two-Dimensional Electrons in a Perpendicular Magnetic Field, Phys. Rev. Lett. **89**, 226805 (2002).
[33] J. Isberg, M. Gabrysch, J. Hammersberg, S. Majdi, K. K. Kovi, and D. J. Twitchen, Generation, transport and detection of valley-polarized electrons in diamond, Nat. Mater. **12**, 760 (2013).
[34] Z. Zhu, A. Collaudin, B. Fauqu, W. Kang, and K. Behnia, Field-induced polarization of Dirac valleys in bismuth, Nat. Phys. **8**, 89 (2012).
[35] Y. Shimazaki, M. Yamamoto, I. V. Borzenets, K. Watanabe, T. Taniguchi, and S. Tarucha, Generation and detection of pure valley current by electrically induced Berry curvature in bilayer graphene, Nat. Phys. **11**, 1032 (2015).
[36] W. Yao, D. Xiao, and Q. Niu, Valley-dependent optoelectronics from inversion symmetry breaking, Phys. Rev. B **77**, 235406 (2008).
[37] T. Cao, G. Wang, W. Han, H. Ye, C. Zhu, J. Shi, Q. Niu, P. Tan, E. Wang, B. Liu, and J. Feng, Valley-selective circular dichroism of monolayer molybdenum disulphide, Nat. Commun. **3**, 887 (2012).
[38] H. Zeng, J. Dai, W. Yao, D. Xiao, and X. Cui, Valley polarization in MoS_2 monolayers by optical pumping, Nat. Nanotechnol. **7**, 490 (2012).
[39] K. F. Mak, K. He, J. Shan, and T. F. Heinz, Control of valley polarization in monolayer MoS_2 by optical helicity, Nat. Nanotechnol. **7**, 494 (2012).
[40] A. M. Jones, H. Yu, N. J. Ghimire, S. Wu, G. Aivazian, J. S. Ross, B. Zhao, J. Yan, D. G. Mandrus, D. Xiao, W. Yao, and X. Xu, Optical generation of excitonic valley coherence in monolayer WSe_2, Nat. Nanotechnol. **8**, 634 (2013).
[41] J. R. Wallbank, A. A. Patel, M. Mucha-Kruczyński, A. K. Geim, and V. I. Fal'ko, Generic miniband structure of graphene on a hexagonal substrate, Phys. Rev. B **87**, 245408 (2013).
[42] P. Moon and M. Koshino, Electronic properties of graphene/hexagonal-boron-nitride moiré superlattice, Phys. Rev. B **90**, 155406 (2014).
[43] Y. Du, N. Xu, X. Lin, and A.-P. Jauho, Moiré effects in graphene-hBN heterostructures, Phys. Rev. Research **2**, 043427 (2020).

[44] D. S. Abergel, J. Wallbank, X. Chen, M. Mucha-Kruczyński, and V. I. Fal'Ko, Infrared absorption by graphene-hBN heterostructures, New J. Phys. **15**, 123009 (2013).

[45] Z. Shi, C. Jin, W. Yang, L. Ju, J. Horng, X. Lu, H. A. Bechtel, M. C. Martin, D. Fu, J. Wu, K. Watanabe, T. Taniguchi, Y. Zhang, X. Bai, E. Wang, G. Zhang, and F. Wang, Gate-dependent pseudospin mixing in graphene/boron nitride moiré superlattices, Nat. Phys. **10**, 743 (2014).

[46] D. S. L. Abergel and M. Mucha-Kruczyński, Infrared absorption of closely aligned heterostructures of monolayer and bilayer graphene with hexagonal boron nitride, Phys. Rev. B **92**, 115430 (2015).

[47] A. M. DaSilva, J. Jung, S. Adam, and A. H. MacDonald, Terahertz conductivity of graphene on boron nitride, Phys. Rev. B **92**, 155406 (2015).

[48] L. Liu, Y. P. Feng, and Z. X. Shen, Structural and electronic properties of *h*-BN, Phys. Rev. B **68**, 104102 (2003).

[49] R. Kubo, Statistical-mechanical theory of irreversible processes. I. General theory and simple applications to magnetic and conduction problems, J. Phys. Soc. Jpn. **12**, 570 (1957).

[50] Y. Tatsumi, K. Ghalamkari, and R. Saito, Laser energy dependence of valley polarization in transition-metal dichalcogenides, Phys. Rev. B **94**, 235408 (2016).

[51] K. Ghalamkari, Y. Tatsumi, and R. Saito, Energy band gap dependence of valley polarization of the hexagonal lattice, J. Phys. Soc. Jpn. **87**, 024710 (2018).

[52] M. Akita, Y. Fujii, M. Maruyama, S. Okada, and K. Wakabayashi, Momentum-selective optical absorption in triptycene molecular membrane, Phys. Rev. B **101**, 085418 (2020).

[53] T. Ando, Y. Zheng, and H. Suzuura, Dynamical conductivity and zero-mode anomaly in honeycomb lattices, J. Phys. Soc. Jpn. **71**, 1318 (2002).

[54] M. Koshino, Stacking-dependent optical absorption in multilayer graphene, New J. Phys. **15**, 015010 (2013).